PROCEEDINGS, 48th Workshop on Geothermal Reservoir Engineering
Stanford University, Stanford, California, February 6-8, 2023
SGP-TR-224

Temperature Uncertainty Modeling with Proxy Structural Data as Geostatistical Constraints for Well Siting: An Example Applied to Granite Springs Valley, NV, USA

Whitney Trainor-Guitton[1], Drew Siler[2], and Bridget Ayling[3]

[1]National Renewable Energy Laboratory, 15013 Denver West Parkway, Golden, CO 80401

Whitney.TrainorGuitton@nrel.gov

[2]previously USGS, currently Geologica, 75 Caliente St., Reno, NV 89509

dsiler@geologica.net

[3]Univ. of Nevada-Reno, Reno, NV

bayling@unr.edu

Keywords: geostatistics, 3D temperature modeling, entropy, drilling decisions

ABSTRACT

Utilizing existing temperature and structural information around Granite Springs Valley, Nevada, we build 3D stochastic temperature models with the aim of evaluating the 3D uncertainty of temperature and choosing between candidate exploration well locations. The data used to support the modeling are measured temperatures and structural proxies from 3D geologic modeling, the latter considered "secondary" data. Two stochastic geostatistical techniques are explored for incorporating the structural proxies: cosimulation and local varying mean.

With both the cosimulation and local varying mean methods, many equally likely temperature models (i.e., realizations) are produced, from which temperature probability profiles are calculated at candidate well locations. To aid in choosing between the candidate locations, two quantities summarize the temperature probabilities: V_{prior} and entropy. V_{prior} quantifies the likelihood for economic temperatures at each candidate location, whereas entropy identifies where new information has the most potential to reduce uncertainty.

In general, the cosimulation realizations have smoother spatial structure, and extrapolate high temperatures at candidate locations that are located along the direction of the longest spatial correlation, which are down dip from existing temperature logs. The smooth realizations result in tight temperature probability profiles that are easier to interpret, but they have unrealistic temperature reversals in some locations because the cosimulation technique does not enforce a conductive geothermal gradient as a baseline (i.e., linearly increasing temperature with depth). The local varying mean results produce realizations with more realistic geothermal gradients, with temperatures increasing downward since a depth-temperature relationship is included. However, because they have much noisier spatial nature compared to cosimulation, it is harder to interpret the temperature probability profiles. The different local varying mean results allow the geologist to determine which proxy (e.g., dilation versus distance to fault termination) should be used given the specific geothermal system. In general, V_{prior} from local varying mean results identify locations that are close to high values for the structural proxies: areas with higher probabilities for higher temperatures. The entropy results identify where uncertainty is greatest and therefore new drilling information could be most useful. Though these techniques provide useful information, even when applied to areas of sparse data, our comparison of these two techniques demonstrates the need for new geothermal geostatistics techniques that combine the advantages of these two methods and that are tailored to the spatial uncertainty issues inherent in geothermal exploration.

1. INTRODUCTION

Prospecting for hidden geothermal resources is challenging. In areas where no surficial evidence indicates that heat, fluids, and permeability may coexist at depths that can be economically drilled, many inferences must be made. Geothermal play fairway analysis has provided a means for combining diverse regional data types and geologic observations into likelihoods of geothermal resources at the regional scale, allowing for discovery of potential and previously unknown hidden geothermal resources. Generally, play fairway analysis has been very successful in identifying hidden prospects via 2D regional analysis (Faulds et al., 2015b, 2017).

After a geothermal prospect is identified, the next stage is discovery, where the goal is to delineate how hot and large the resource is by refining the conceptual geothermal model; ultimately, these models are then used to determine the power capacity (Cumming, 2016a, 2016b; Craig et al., 2021). This stage includes well-siting decisions to prove the resource and/or refine the hypotheses around the system (e.g., reservoir geometry, hydrothermal upflow/outflow pathways, and spatial distribution of subsurface temperatures). Determining where to collect deeper temperature observations, such as drilling thermal gradient holes (TGH), is a difficult decision: TGHs drilled at finite locations may confirm that economic temperatures exist *and/or* provide evidence to either prove or disprove current conceptual models of the geologic structure or geothermal processes. Herein lies an important theme of the work presented: temperature measurements provide a direct measure of heat albeit at finite 3D locations, whereas geologic modeling can give spatially extensive indications of proxy measurements for temperature.

Various geological and geophysical datasets are often used as proxies for one or more of the three components needed for conventional geothermal systems: fluids, permeability, and heat. Fault mapping can reveal possible permeability pathways for deeper, hotter fluids to

travel towards the surface (Faulds et al., 2010, 2015a). Three-dimensional mapping of these geologic features brings more geologic realism to the representation and understanding of the subsurface geologic complexity and its control on permeability (Witter et al., 2019; Siler and Pepin, 2021).

Geothermal conceptual modeling has not historically employed 3D stochastic modeling, which would provide robust probabilistic results to the subsurface temperature distribution, while also adhering to spatial correlations observed in the data. Whereas earth scientists in mineral and petroleum applications have utilized geostatistics to generate spatial models quantitatively and probabilistically, geostatistics has a long history of spatial interpolation of sparsely sampled earth science data (Journel and Huijbregts, 1978; Deutsch and Journel, 1998). Geostatistical interpolation often uses the variogram, which 1) quantifies the spatial correlation of the property of interest (e.g., porosity, permeability, temperature) and 2) can be used to inform spatial interpolation, known as Kriging. Williams and DeAngelo (2011), one of the first published studies using Kriging for geothermal applications, compared 2D Kriging to spline estimations for both heat, flow and temperature at discrete depths.

In this study, we apply 3D stochastic geostatistical techniques that utilize both direct and proxy measurements of temperature to help inform exploration decision-making, where the information available is representative of the discovery stage: 2-meter temperature probes and a handful of deeper temperature gradient measurements exist along with 3D models of temperature proxies. Specifically, we explore these geostatistical methods with the Granite Springs Valley geothermal system located in Nevada, USA, which is one of the prospects identified through regional play fairway analysis (Faulds et al., 2019). Substantial existing data are available for this resource prospect, including six thermal gradient wells (<260m deep), gravity, magnetotellurics, and seismic data that allowed for 3D geologic modeling (Ayling et al., 2022). However, additional drilling is required to test resource conceptual models and evaluate the most likely hydrothermal upflow location for the system. At Granite Springs Valley, nine candidate locations for new TGH wells have been identified that would test the proposed isotherms of the different conceptual models (e.g., P10/optimistic, P50, and P90/pessimistic).

We present and compare two quantitative workflows, cosimulation and local varying mean, to aid in choosing future drill sites for TGHs at Granite Springs Valley (Figure 1) and ideally for other geothermal prospects at the discovery stage. Both workflows combine directly observed temperatures and inferred but spatially extensive geologic proxies to temperature. These workflows represent the first stochastic temperature modeling, which utilizes calculated and spatially extensive proxies related to the inferred location of faults and stress/strain-related proxies for permeability. Specifically, the methodology utilizes many equally probable 3D temperature models to calculate the probability of temperature at any location in the 3D subsurface. These temperature probabilities are then summarized into two quantities: prior value (V_{prior}) and entropy (H). V_{prior} and entropy are calculated from these results and are useful to balance the two objectives of 1) confirming high temperatures and 2) improving knowledge of the subsurface with the new TGH at Granite Springs Valley. Thus, the paper begins by providing two example calculations of V_{prior} and entropy, then describes the two stochastic geostatistical techniques. The results section describes these modeling techniques applied to Granite Springs Valley. We conclude the paper with discussion of the results and potential improvements to the workflow for future application to other greenfield prospects.

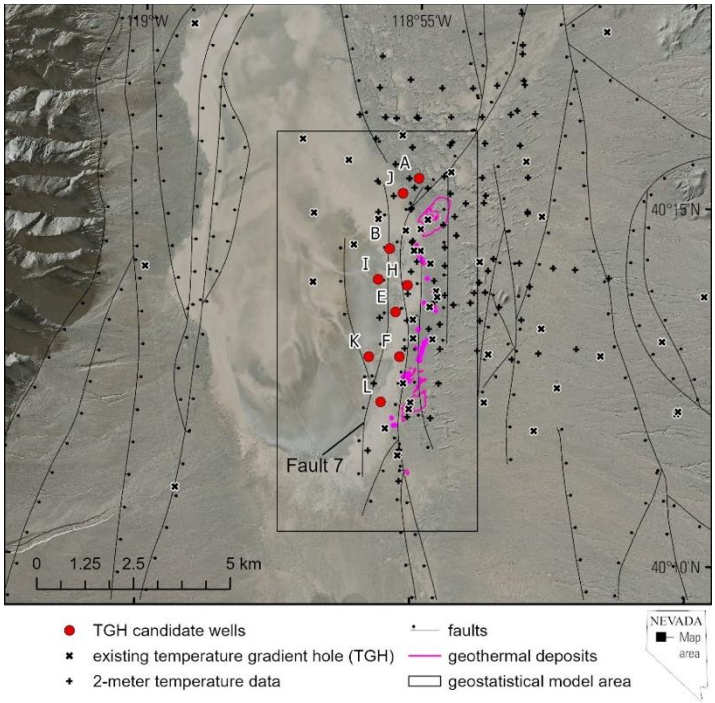

Figure 1: Map of northern Granite Springs Valley geothermal area. The local 2-m temperature data and TGH temperature data are shown, though only temperature data within the geostatistical model area are used in the analyses.

2. GEOSTATISTICAL METHODS & SUMMARY METRICS OF VPRIOR & ENTROPY

In this section, we introduce V_{prior} and entropy to motivate the stochastic geostatistical modeling. We then briefly describe Kriging, the variogram, and stochastic simulation. Lastly, we introduce the two methods that allow geologic proxies to be included in the stochastic temperature modeling: cosimulation and local varying mean.

2.1 Vprior & Entropy

The prior value (V_{prior}) identifies the action that results in the highest utility given many uncertain scenarios. For the geothermal drilling example, we can make a simplifying assumption that our decision outcome is determined mostly by temperature (T). Thus, a V_{prior} expression could be

$$V_{prior}(\boldsymbol{u}) = \max_{a}\left[\sum_{i=1}^{Ntemp_{bins}} \Pr\big(T = t_i(\boldsymbol{u})\big)\, v_a\big(T = t_i(\boldsymbol{u})\big)\right];\ a = \{\text{drill}, \text{don't drill}\} \quad (1)$$

where the sum represents a weighted average (e.g., expected value) over the temperature bins (t_i), $Ntemp_{bins}$ is the number of temperature classes (eight here), $\boldsymbol{u}$ is position vector, and v_a represents the utility outcome (often in turns of monetary units) of some decision action a, which could be to drill a TGH or not. The weights for each temperature bin are expressed with the probability Pr(.). **To explore our chances of drilling success (which may be defined by intersecting hot temperatures), we want to obtain the probability of the temperature classes occurring in the 3D subsurface, utilizing all the current information available to us today.**

The other quantity explored to identify where to drill new wells is entropy, which addresses a very different drilling objective from V_{prior}. Entropy quantifies statistical disorder, and specifically in this study how the temperature probabilities are distributed among the temperature classes. The following equation is the Shannon entropy (Shannon, 1948) value at each location, u, on the basis of the class probabilities $\Pr(T = t_i)$:

$$H(u) = -\sum_{i=1}^{Ntemp_{bins}} \Pr(T = t_i(u)) \log_2 \Pr(T = t_i(u)) \quad (2)$$

Entropy is reduced (e.g., statistical disorder reduced) when one class has a higher probability relative to the other classes. If we use V_{prior} to site new wells, the drilling objective is to find economic temperatures. Conversely, by targeting locations in the model that have high entropy locations, we aim to reduce disorder: by collecting new data in those areas and adding the newly acquired temperature data to the model the entropy would then be reduced, and future models would be better constrained. In other words, areas of higher entropy are locations where new information has the most potential to reduce uncertainty.

2.2 Stochastic 3D Geostatistics, Including Temperature Proxy Information

In order to make spatial decisions about where to drill using V_{prior} and entropy in the 3D subsurface, we must explicitly represent all the locations ($\boldsymbol{u}$) and define their respective temperature class probabilities $\Pr(T = t_i(\boldsymbol{u}))$. Stochastic geostatistics provides methods for making these spatial inferences. The language here will speak specifically to temperature data, but the equations are general and applicable to any spatial data type.

Kriging is sometimes referred to as geologically based spatial interpolation, because through the variogram, modelers can impose which direction(s) have higher spatial correlation. Experimental variograms are calculated from observed data, but when data are very sparse, geologic modelers can supplement this with their geologic knowledge of the area (e.g., depositional trends, structural tendencies, or stress orientations). Kriging interpolation uses the variogram/covariance to determine how much weight to put on each observed data point when calculating the value at each unsampled location. So unlike inverse distance weighting, Kriging will give more weight to data that are in the direction with lower dissimilarity, or higher spatial continuity (Webster and Oliver, 2008), and importantly, this allows for data that are aligned with geologic trends to have more impact on estimated values. Stochastic simulation techniques combine the Kriging interpolation methods, with Monte Carlo sampling to produce many different, but equally likely models that match the observed measurements and reproduce the variogram.

Geostatistical methods allow for the inclusion of secondary data that may also constrain the quantity of interest (here temperature) in addition to primary data. The secondary data are typically used to capture larger spatial trends of the main property (Chilès and Delfiner, 2012; Remy et al., 2011). Commonly, the secondary data are geophysical or remote-sensing data (Gloaguen et al., 2005, 2007; Hansen et al., 2006). Recently, other less conventional data have been used as secondary data, such as geologic interpretations of lithofacies (Boyd et al., 2020). We explore two possible methods for including secondary information: cosimulation and local varying mean (LVM). Cosimulation represents the secondary data as discrete or finite data locations and incorporates them via variogram analysis, similar to Kriging. LVM uses secondary information to describe how the mean of the primary data (e.g., temperature data) changes in space.

2.2.1 Cosimulation

Like stochastic simulation for Kriging, cokriging can be used to produce stochastic results. This is called cosimulation. The theory and Kriging expressions are flexible to allow the data $T(u_\alpha)$ and the unknown $T^*_{SK}(\boldsymbol{u})$ to be different attributes. Commonly, the estimation of porosity has been informed by ancillary data such as seismic amplitude data (Ferreira and Lupinacci, 2018). Cokriging provides an

extension of Kriging where data of different attributes can be used to make estimations of a property of interest, in our case temperature. The simple cokriging equation for an unsampled temperature location $\boldsymbol{T_1^*(u)}$ is as follows

$$\boldsymbol{T_1^*(u)} - m_1 = \sum_{\alpha=1}^{n_1(u)} \lambda_\alpha [T_1(\mathbf{u_\alpha}) - m_1] + \sum_{\beta=1}^{n_2(u)} \lambda_\beta [T_2(\mathbf{u'_\beta}) - m_2] \quad (3)$$

where $n_1(u)$ denotes the number of neighboring temperature data $T_1(\boldsymbol{u})$, and $n_2(u)$ is the number of secondary data $T_2(u'_\beta)$. The λ_α and λ_β are the corresponding cokriging weights. The means of the two respective properties are represented by $m_1$and m_2.

2.2.2 Local Varying Mean

Another method for stochastically simulating temperature data while also incorporating secondary information is simulation with local varying mean (LVM). The LVM method utilizes a secondary data set to capture systematic variation in the mean of the property. Typically, the LVM values are derived from aerially extensive remote-sensing data such as seismic reflection. Thus, LVM should 1) have a trend and 2) this trend should be smoothly varying. Equation 4 provides the LVM equation

$$T^*_{LVM}(\mathbf{u}) - m^*(\mathbf{u}) = \sum_{\alpha=1}^{n(u)} \lambda_\alpha^{SK}(u)[T(\mathbf{u}_\alpha) - m^*(\mathbf{u}_\alpha)] \quad (4)$$

where the locally varying mean that is available at all locations is denoted as $m^*(\boldsymbol{u})$. Typically, the secondary variable is transformed through linear regression into the local mean of the primary attribute. This differs from the cosimulation method, which integrates the information through covariances (via variogram).

Therefore, the secondary data $T_2(\mathbf{u'_\beta})$ may need to 1) be interpolated to be represented at all locations $T_2(\mathbf{u})$ and 2) be regressed to the parameter of the primary data using collocated primary data

$$t_1(\mathbf{u_\alpha}) = a\, t_2(\mathbf{u_\alpha}) + b \quad (5)$$

which regression parameters, a and b, can be used on the interpolated secondary data to define the local varying mean $m^*(\boldsymbol{u})$

$$m^*(\mathbf{u}) = a\, t_2(\mathbf{u}) + b \quad (6)$$

3.0 RESULTS: STOCHASTIC TEMPERATURE MODELING AT GRANITE SPRINGS VALLEY

This section presents the results of the described methods applied to Granite Springs Valley, NV. The northern Granite Springs Valley geothermal area is located in northern NV, ~140 miles northeast of Reno. Granite Springs Valley hosts a shallow thermal anomaly defined by 47 shallow (15-550 m) TGH datasets, largely from exploration efforts in the 1970s (Benoit, 2012). In more recent research, Granite Springs Valley emerged from the Nevada Play Fairway project (2016-2019) as a particularly prospective blind geothermal resource (Faulds et al., 2017, 2019, 2021). As part of this effort, opaline silica sinter, silicified lacustrine sediments, and travertine were discovered cropping out discontinuously along a ~6 km (north-south) profile adjacent to the thermal anomaly (Figure 1). Associated geophysical and geological studies informed a six well thermal gradient drilling campaign. Maximum temperatures of 96°C at 150-250 m depth and 77.7°C at 150 m depth were encountered at the northern and southern extents of the surface geothermal deposits, respectively. The geostatistical analyses herein will contribute to decision-making about future TGH drilling in this area.

First, the model volume, the temperature (primary) data, and their respective 3D variogram calculations are described. Next the secondary data originating from the geologic conceptual model and their geomechanical/stress calculations and the Principal Component Analysis calculations to combine them are described. This information is used as a secondary constraint in the 3D stochastic temperature modeling, which is performed in the open source SGEMS software (Remy et al., 2011). Finally, the 3D modeling results, the 1D probability profiles extracted at the candidate well locations, and their respective V_{prior} and entropy measurements are presented.

3.1 Existing Temperature Data & Their 3D Variogram

A 5,175 m (easting) by 10,350 m (northing) by 800 m (depth) volume in the Granite Springs Valley area is the focus of 3D geostatistical modeling. This volume centers around the existing temperature observations (Figure 2). Given the elevation of Granite Springs Valley (~1200 m), the model domain reaches 300 m of elevation. This represents the likely depths for the next drilling campaign. Geostatistical interpolation is bounded by what was understood to be the principal western fault, therefore no temperatures west of this fault were used or interpolated, assuming that statistical stationarity is not valid across the fault. Also shown in Figure 2 is what was interpreted as the main eastern fault in the area. The grid size is 69x138x90 cells such that each cell represents 75x75x10 m. The higher depth resolution represents the importance of capturing temperature trends in depth. The figures that follow with the temperature modeling results represent the same volume (UTM and elevation) as Figure 2.

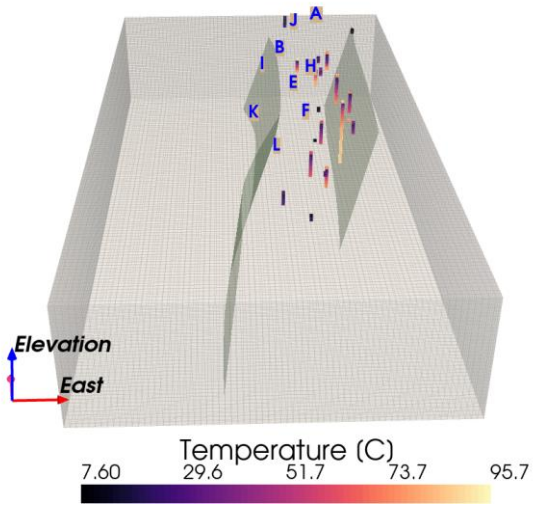

Figure 2: Geostatistical modeling volume with 2 faults (green) from the Granite Springs Valley conceptual model, the temperature data projected onto well traces, and the 9 candidate well locations (labeled with blue letters)

We utilize both the existing 2-meter temperature and the vertical temperature data for the 3D variogram calculation and subsequent geostatistical model generation. The left plot in Figure 3 is the histogram of the observed temperature data, where the peak around 20°C is from the 2-meter measurements, the most common data type. The hottest temperatures are from the deep vertical logs that reach up to 550 m depth (around 600 m above sea level). Given the occurrence of opaline sinter (suggestive of reservoir temperatures >175°C) and geothermometry suggesting reservoir temperatures of ~140°C, it was deemed reasonable to extrapolate to 140°C during the data transformation stage such that each 3D model will have a temperature distribution that closely resembles the histogram on the right in Figure 3.

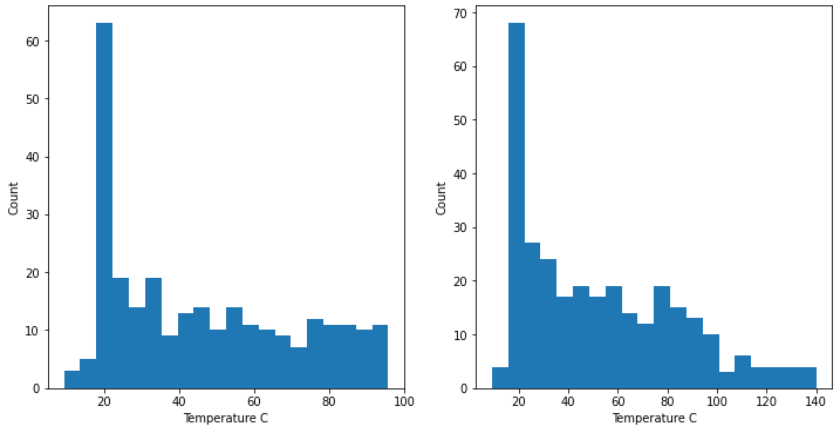

Figure 3: Left: distribution of observed Granite Springs Valley temperatures in the 2-m and vertical logs. Right: extrapolation used to put highest temperatures at 140°C in all 3D temperature realizations

Figure 4 contains four directional variograms of the temperature data: north-south, vertical, northeast (N45E), and east-west. The red marks depict the temperature data variograms in all but the vertical variogram; there is also a continuous black line depicting the modeled variogram in that direction. Variograms are insightful in determining which direction the data have more correlation or change the slowest; this is captured partially by the range: the distance (x-axis) at which the variogram asymptotes to the highest dissimilarity value (sill value on y-axis). The roughly interpreted value of the range for the four directions is depicted in Figure 4, except for the vertical direction, which we will discuss below. The data variograms are influenced by the configuration of which the data are sampled. For instance, as seen in Figure 2, most measurements are collected along the north-south direction. Therefore, it is imperative to combine the raw variogram calculations with geologic knowledge of the area, which is done by fine-tuning the 3D variogram model that ultimately goes into the geostatistical modeling.

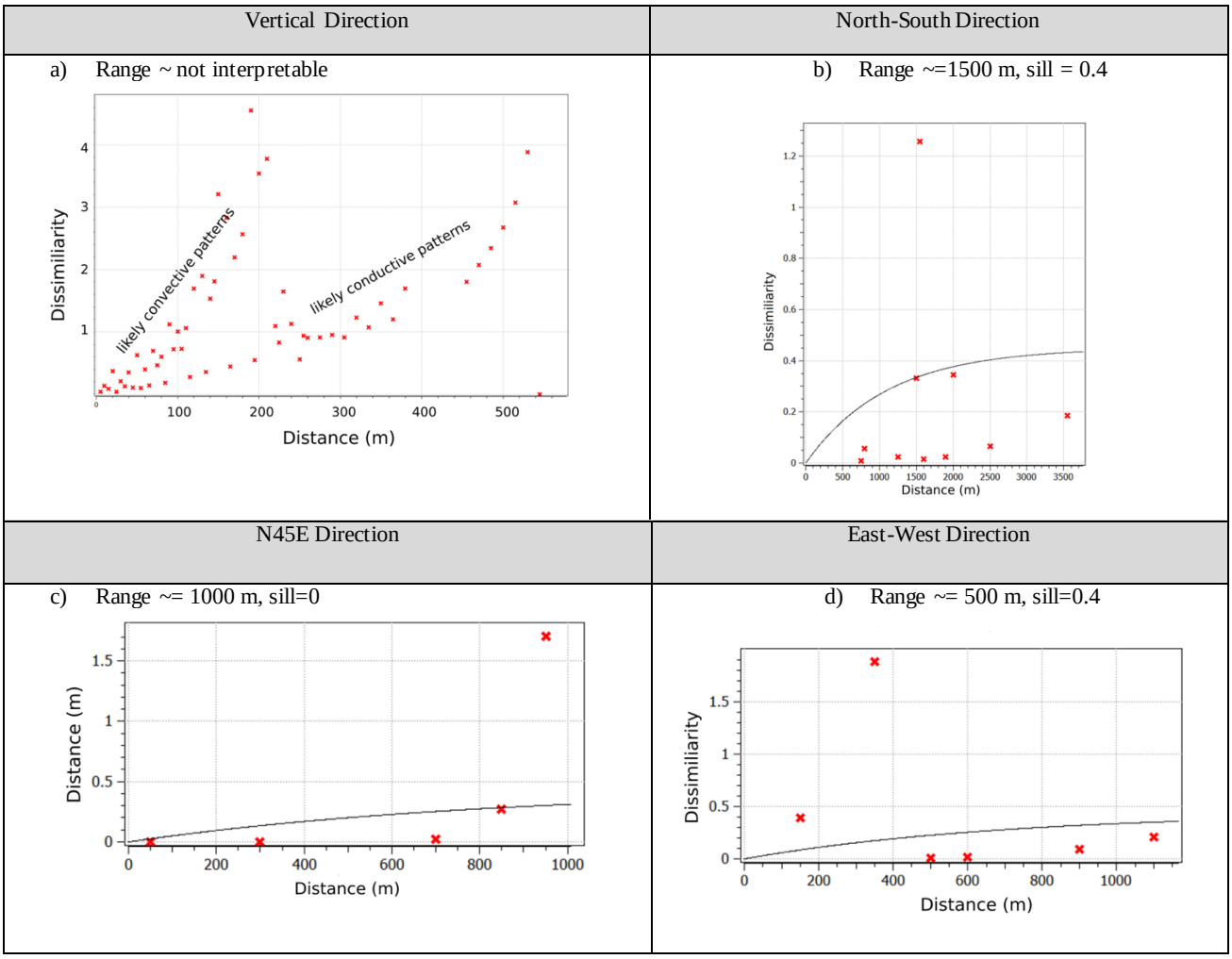

Figure 4: Four directional variograms informed by the 16 vertical temperature logs and 2-m temperatures: a) north-south direction with range about 1,500 m and b) vertical temperature variogram. The conduction versus convection trends are clear in the two spatial dissimilarity trends. c) 45 degree range ~ 1,000 m, and d) east-west range is less than 500 m.

The main western fault, seen in Figure 2, is a possible controlling geologic feature for temperature, so we use this to help describe the 3D ellipsoid that is the 3D variogram. The mean strike of the fault is azimuth=000 (north-south), the mean dip is 60°, and the mean dip direction is azimuth=270 (due west); these angles are represented in Figure 5. We expect geothermal fluids to be upwelling up-dip in the fractured rock (high porosity and permeability) near faults, so we use the dip direction (azimuth=270, clockwise from north) and dip (60° from XY plane) of the western fault to define the direction of the major axis. Given the absence of a sill in the vertical variogram, the range for the vertical variogram is chosen to fit the observed range in the north-south direction (the one with the most data). The major radius along the fault strike and dip is set at 2700 m, which when projected into the XY plane is approximately 1,300 m (=2,700*cosine(60°)), matching roughly what is observed in the north-south variogram (Figure 4a). After some initial testing in the geostatistical realizations, the medium axis is the fault strike direction [azimuth=000 (north-south), dip = 0° (horizontal)], and minimum axis is orthogonal to the fault plane (azimuth=270, dip -30 normal to the fault plane). The radii for the medium and minimum axes are set to 500 m, which is consistent with the angles seen in Figure 4.

Table 1 summarizes the 3D variogram that was fit to the measured temperature data. In the table are the three radii of the ellipsoid and the direction in which the maximum direction of correlation is oriented (max radius). Also, the table shows that a Gaussian variogram is chosen, which describes a property that changes slowly at small spatial scales, which is appropriate for the property of temperature given the physical processes of diffusion. Other variogram types (e.g., exponential or spherical) would impose more abrupt changes at very short spatial scales. The variogram model has no nugget effect, again to prevent these discontinuities at short distances in the interpolated models.

Table 1: The parameters (direction, ranges, and type) of the primary variogram (fit to measured temperature data)

GUASSIAN, NUGGET=0	MAX	MEDIUM	MIN
RANGES (meters)	2,730	500	500
	Azimuth	Dip	Rake
ANGLES (degrees)	270	-60	0

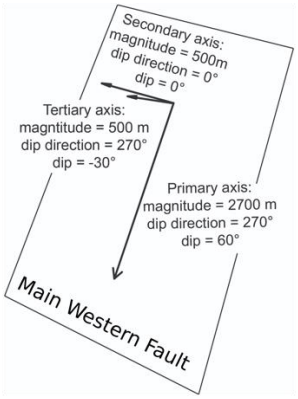

Figure 5: Conceptual cartoon showing main western fault and the radii of the primary variogram

3.2 Secondary Data: Temperature Proxies from Geologic Modeling

Conceptual geologic modeling has become an increasingly important step in discovering and/or understanding geothermal fluid circulation (Siler et al., 2018; Siler and Pepin, 2021). At Granite Springs Valley, 3D geologic analyses are used to produce four quantities: distance to fault, distance to fault intersection (Siler and Faulds, 2013; Siler and Pepin, 2021), Coulomb shear stress change, and dilation (Siler et al., 2018). Faults and fault intersections are important structures that can produce permeability, which then can allow for pathways for geothermal upwelling, so the distance to faults and distance to fault intersection are reasonable proxies for high temperatures, i.e., they are likely loci of convective heat transport. The dilation and coulomb shear stress change proxies are modeled stress and strain effects of fault slip. Areas that undergo high dilation and high coulomb shear stress change are prospective areas for geothermal processes, since they represent long-lived areas of permeability generation and maintenance (Siler et al., 2018). These are shown in Figure 6.

Secondary data is incorporated via the Markov-Bayes method, in which correlation coefficients between the four proxy parameters and the measured temperatures are calculated. Only proxy values that are within 100 m of a measured temperature are used. A weighted correlation coefficient is used to give more weight to deeper measurements as they may be closer to geologic features. The weighted correlations are shown in Table 2. The last row and column contain the correlations of the temperatures and the four proxies, none of which are very strong. The two fault proxies (distance to fault and fault intersections) are somewhat correlated at 0.63, and the two stress-related proxies have a high anti-correlation of -0.86.

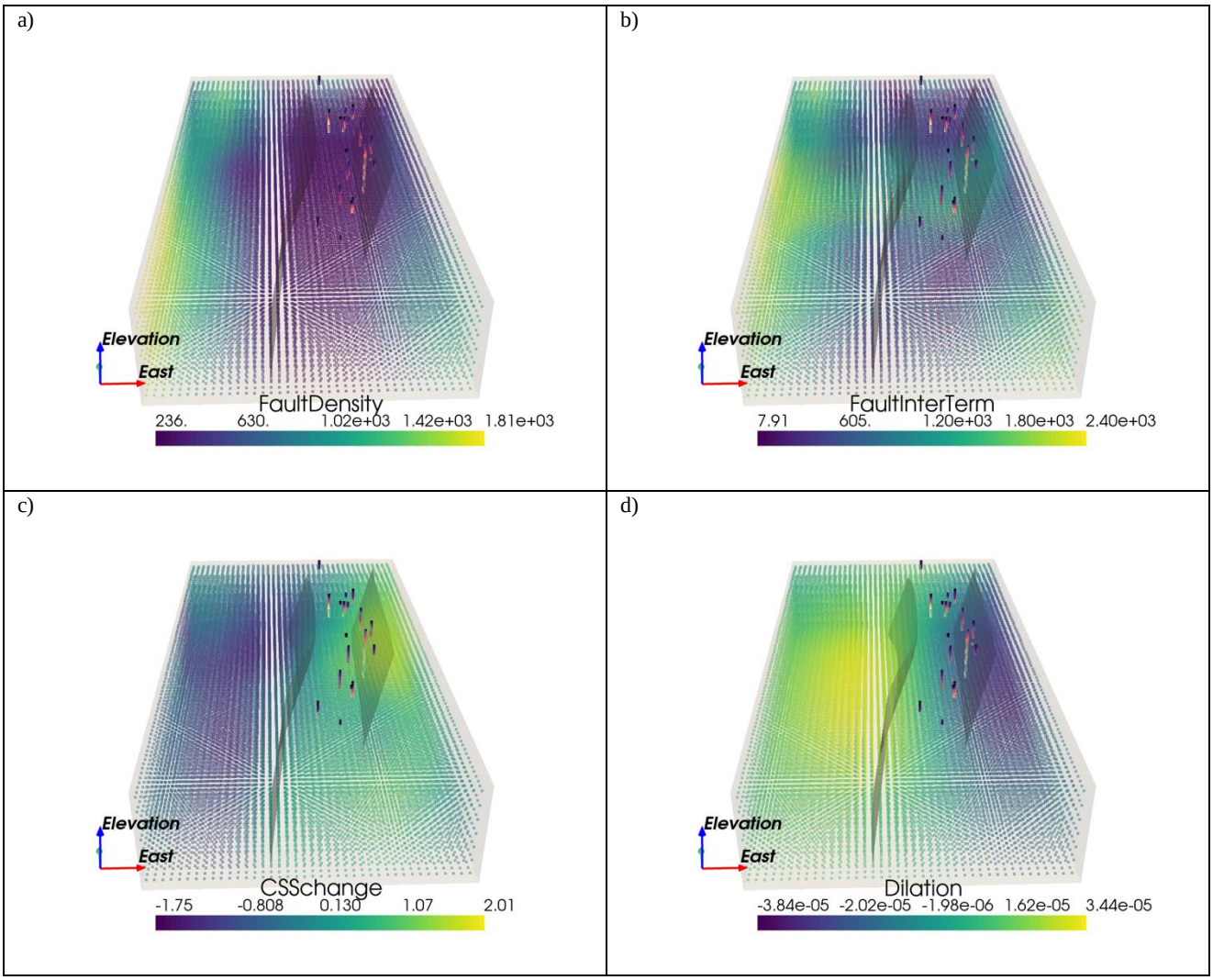

Figure 6: Temperature-proxies a) distance to fault b) distance to fault intersections/terminations c) Coulomb shear stress (CSS) d) dilation tendency

Table 2: Correlation coefficient table for the four secondary data (proxies for temperature) and the measured temperature (last column). The two fault related proxies are well correlated at 0.63, and the stress parameters are inversely correlated at -0.86.

	Distance to Fault	Distance to Fault Intersections	Coulomb Stress Change	Dilation	Measured Temperature
Distance to Fault	1	0.63	-0.34	0.183	0.29
Distance to Fault Intersections	0.63	1	-0.31	0.22	0.21
Coulomb Stress Change	-0.34	-0.31	1	-0.86	0.35
Dilation	0.18	0.22	-0.86	1	-0.56
Measured Temperature	0.29	0.29	0.35	-0.56	1

These correlation coefficients are one way to check how these proxy parameters compare to relatively "collocated" temperature measurements (here defined as within 100 m), but they are not a definitive way to assess which one of these four proxies is best to use. These collocated relationships are highly influenced by where the temperatures were collected. In general, the temperature measurements

are further from the fault intersection values than they are for the distance to fault. Therefore, in general, sampling bias or lack of sampling of the sparse temperature data will affect how we perceive the relationship of these proxies to temperature.

3.2.1 PCA Results

The principal component analysis (PCA) is performed twice: on the two fault proxies (distance and distance to termination) and the two stress proxies (Coulomb stress and dilation). The explained variance ratios of 0.8 and 0.9 by the first principal component for the fault and stress proxies, respectively, indicate that PCA is successful at dimensionality reduction. We continue with the magnitude of these two PCA1 (first component of two different pairs of proxies) as our secondary data. We will refer to these from now on as PCA1 Fault (which combines the distance to faults and distance to intersections and terminations) and PCA1 Stress (which combines the Coulomb stress change and dilation tendency), which are used to produce two separate cosimulation results.

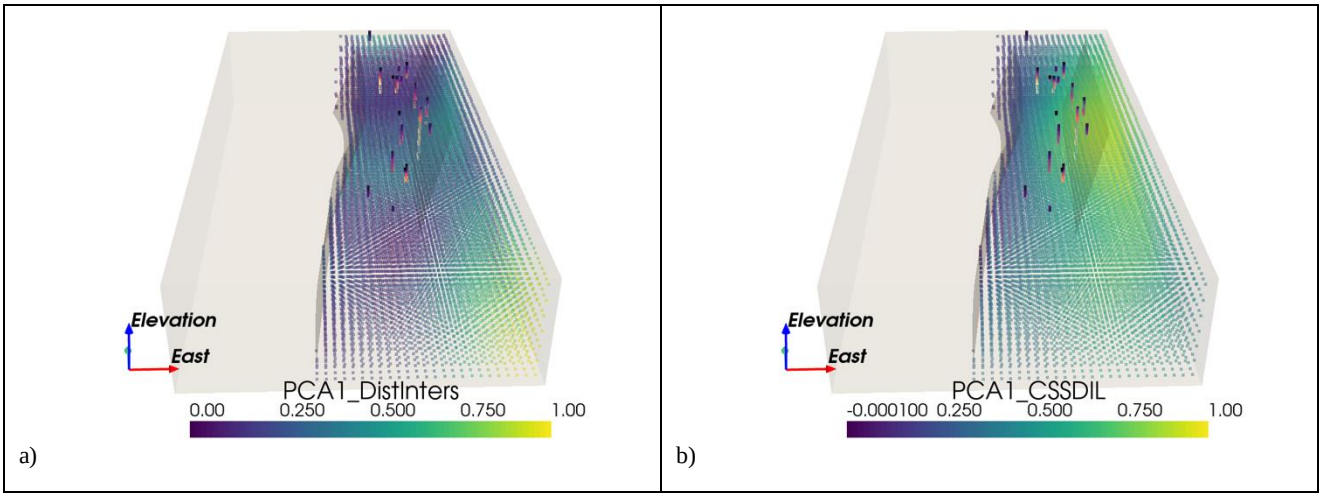

Figure 7: The first principal component for the a) fault proxies and b) stress proxies with original density

In Figure 7, the PCA1 Fault (left side) diverges from the PCA1 Stress (right side) in magnitude in the north-east region of our model volume. However, there is also a relatively high density of temperature measurements in this area, which have more influence on the interpolated values than the secondary data. None of the candidate well locations are in the area where the fault and stress proxies diverge the most (Figure 2).

3.2.2 Local Varying Mean (LVM) Calculations

As described in Subsection 2.4.2, LVM is derived from a secondary source, but must be in terms of the primary data, temperature, and also must be exhaustively available within the simulation area (unlike secondary data in cosimulation which can be at limited locations). Interpolations of the four geologic proxies were used to calculate each LVM in terms of temperature using the four regression expressions. We explain later how the spatial nature of the LVM results can partially be explained by the fact that we are using an interpolated version of the proxies.

Additionally, to develop an LVM in terms of temperature from the geologic proxies, four different linear regressions are performed using the same "collocated" temperature measurements (Equations 5 and 6). The resulting coefficient, intercept, and R^2 score for the four geologic proxies are shown in Table 3. The regression was done including the depth of the temperature measurement.

$$\mathrm{t}_1(\mathbf{u}_\alpha) = a\,\mathrm{t}_2(\mathbf{u}_\alpha) + b\,\mathrm{depth}(\mathbf{u}_\alpha) + c \tag{7}$$

where t_2 represents the one of the four different geologic proxies at each location, a and b are the regression coefficients, and c is the intercept. The LVM is then defined by

$$m^*(\mathbf{u}) = a\,\mathrm{t}_2(\mathbf{u}) + b\,\mathrm{depth}(\mathbf{u}) + c \tag{8}$$

This should be considered an advantage of the LVM work, as it can provide a constraint to force the temperatures to increase with depth (i.e., a realistic scenario in a geothermal setting), whereas cosimulation alone will not.

Table 3: Linear regression parameters for solving for temperature with proxies and depth

	Distance to Fault	Distance to Terminations/ Intersections	Coulomb Stress Change	Dilation
Proxy Coefficient (a)	-0.4	-0.03	-3.85	-1.72e+05
Depth Coefficient (b)	0.13	0.16	0.14	0.12
Intercept (c)	204	262.5	198.9	181.8
R^2 Score	0.62	0.68	0.57	0.56

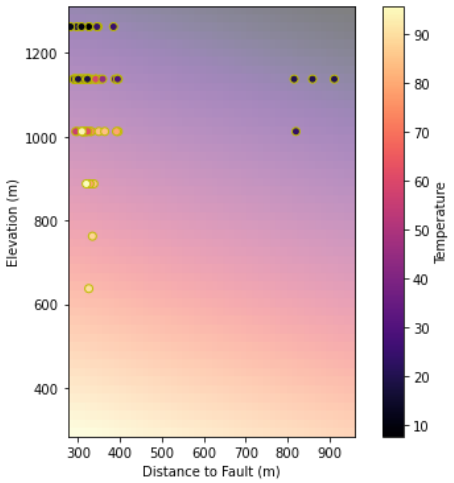

Figure 8: Visual results of the LVM using the distance to fault (DF) secondary data and depth information, with the collocated temperature measurements shown in with scatter points: *LVM* = -0.4 *DF* + 0.13 *Depth* +204

3.3 Example 3D Realizations

This subsection provides the five east-west (X_{min} to X_{max}) slices for two of the 50 3D realizations. The slice views confirm the 60° dip of the primary axis of the 3D variogram. Realizations 25 and 49 are shown for the following three groups: temperature data and PCA1 Fault in cosimulation, temperature data and PCA1 Stress in cosimulation, and finally temperature data with LVM defined with the four different proxies. As a reminder, the difference between the two realizations within each group is the order in which each grid cell is visited as outlined in Section 2.2 and referred to as the "random seed" in the geostatistical parlance. Therefore, the previously simulated values which affect all subsequent temperature draws will differ for each realization.

Figure 9 contains the models created with the temperature data *and* PCA1 Fault component proxies. The high temperature values are centered around the measured hot temperatures and are in shapes given the 3D variogram ellipsoids' orientation and size. The two realizations are consistent with each other, demonstrating that the secondary data has a constraining effect. T**he differences between the realizations are more pronounced the further away they are from temperature measurements.**

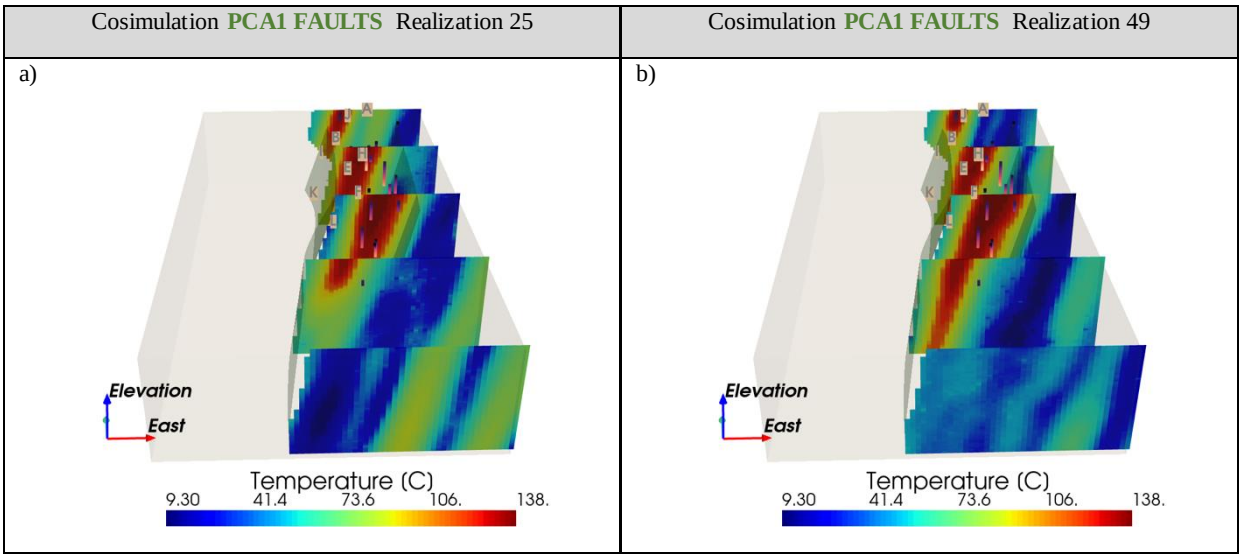

Figure 9: Two example realizations using the PCA1 of Fault proxies: a) Realization 25, b) Realization 49

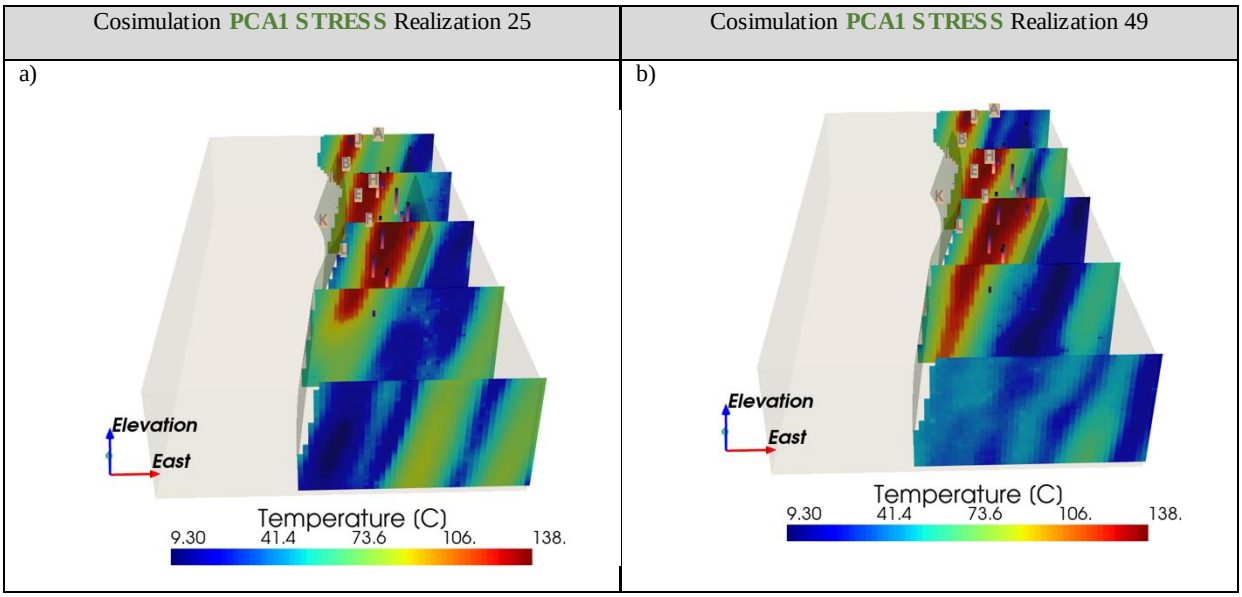

Figure 10: Two example realizations using the PCA1 of Stress proxies: a) Realization 25, b) Realization 49

Figure 10 has the same respective slices and realizations of Figure 9 but using the PCA1 for the Stress proxies. The minimum and maximum difference for all 50 realizations created by the PCA1 Fault and PCA1 Stress is on the order of 10^{-3}°C. The differences in the realizations created from the different PCA1 component are highly influenced by the histogram transformation step. The histogram transformation takes a ranking of each simulated temperature and transforms it into a temperature according to the given distribution; this ends up squeezing the values into smaller spread. Differences between Fault and Stress PCA1 realizations could also be very small because the PCA are normalized between -1 and 1.

The same cross sections and realizations shown for the cosimulations (Figures 9-10) are shown for the LVM simulations in Figure 11, where each row shows the respective LVM derived from the four different proxies: distance to fault, distance to fault intersections and terminations, Coulomb stress, and dilation tendency. The slice views again demonstrate the influence of the 60° dip of the primary axis of the 3D variogram. Compared to the cosimulation results, the LVM realizations place the hotter temperatures deeper in the subsurface, because of the depth being one of two variables used in the LVM linear regression. This is a more realistic scenario for a geothermal system (i.e., temperature generally increase with increasing depth), relative to the cosimulation results. Visually the same realizations across the different proxies (columns of Figure 11) have subtle differences that are controlled by the locations of faults or the estimated stress properties.

	LVM Realization 25	LVM Realization 49
Distance to Fault	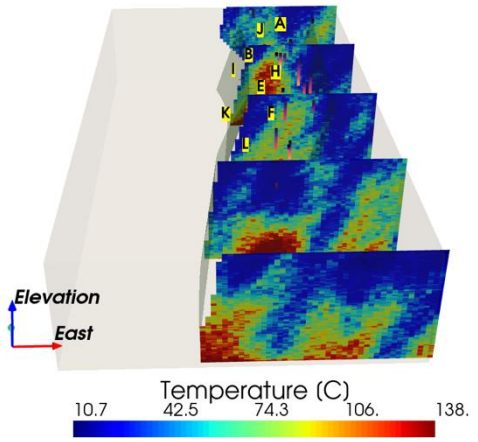	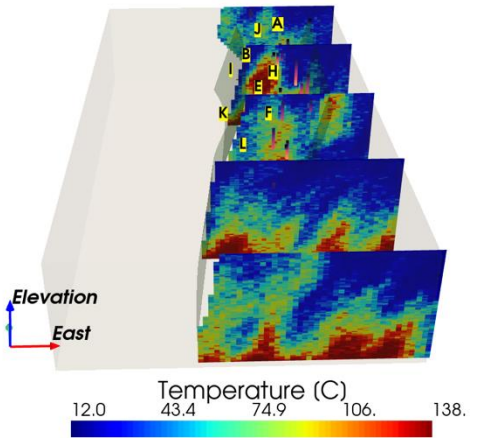
Distance to Fault Intersections	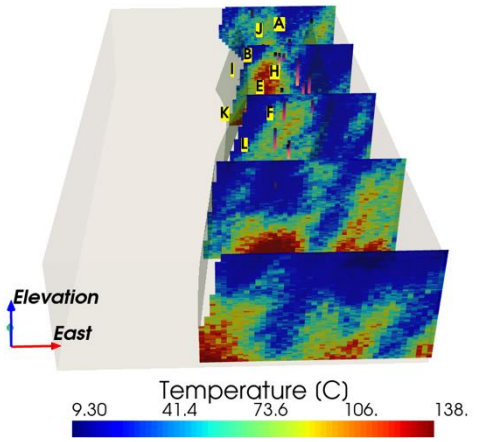	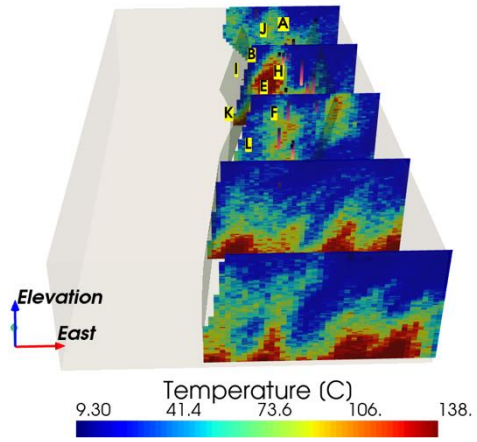
Coulomb Stress Change	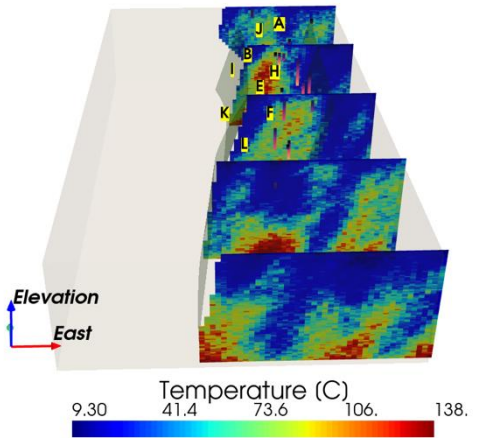	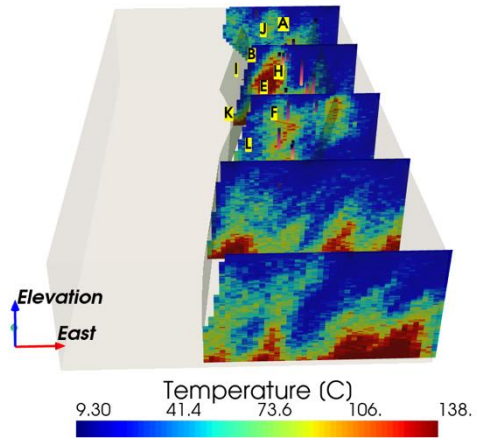

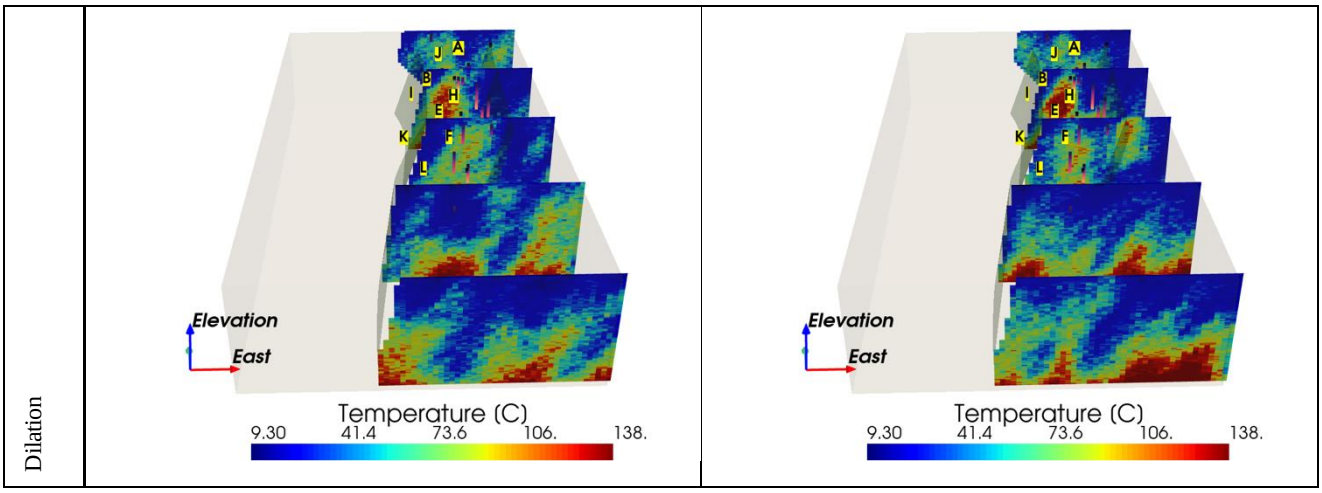

Figure 11: Two example realizations of LVM results using regressions with the four different proxies: distance to fault (top row), distance to fault intersection (2nd row), Coulomb stress (3rd row), and dilation tendency (last row)

3.4 Vertical Profiles at Candidate Well Locations: Temperature Probability Given 50 3D Realizations

The 50 stochastic temperature models within each simulation group are extracted at the 9 candidate well locations, and the probability of temperature bins is calculated for each elevation. These are shown in Figure 12 for the two sets of cosimulations for the fault- and stress-based proxies. Both color scales are set to minimum of 0 and maximum of 30% probability. Candidates I and K are only defined at the very bottom elevations because the well heads are on the west side of the Fault 7 but intersect it at depth, so the upper sections of the wells are outside of the model volume. Also plotted for reference are the temperature profiles for realization 25 (magenta) and 49 (orange), which are the realizations show on Figures 13-14 and 16. The two temperature profiles track close to each other, which explains why the probabilities are relatively tight. A dashed vertical line is plotted at 100°C. Candidates B, E, H, and L seem to have a pattern toward higher temperatures at depth, while A, F, and J do not. The probability patterns are very similar between the two proxy types, which is expected given how similar the realizations are (Figure 9 and Figure 10).

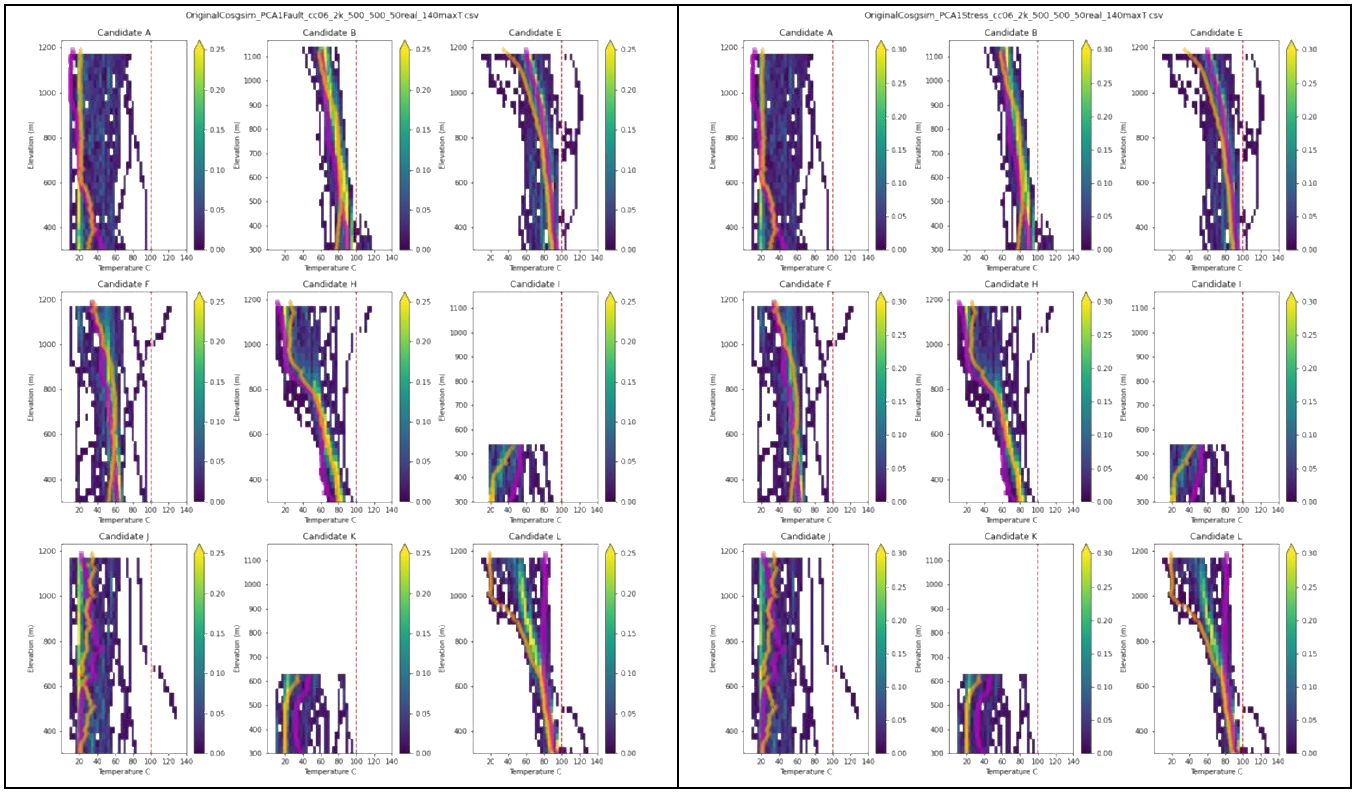

Figure 12: The temperature probability profiles at the 9 candidate well locations for the 2 sets of cosimulations. Color scale is 0-0.3 for all profiles. Magenta and orange lines are from realization 25 and 49, respectively. Left: PCA1 Faults as secondary data; Right: PCA1 Stress as secondary data.

The vertical probability profiles for the four different LVM results are shown in Figure 13 with the same color scale used in Figure 12. The temperature profiles for realizations 25 and 49 are plotted again, which unlike the cosimulation cases are different from each other and have a lot of discontinuity at short depth scales. This contributes to the probabilities being lower and spread out, but there is a slight increase through depth, due to depth being included in the regression calculation. The LVM based on distance to fault seems to have slightly narrower probability range than the distance to fault intersections. In general, it's hard to distinguish the differences between the four LVM probability profiles, but V_{prior} and entropy synthesize these into one number, making it easier to compare them.

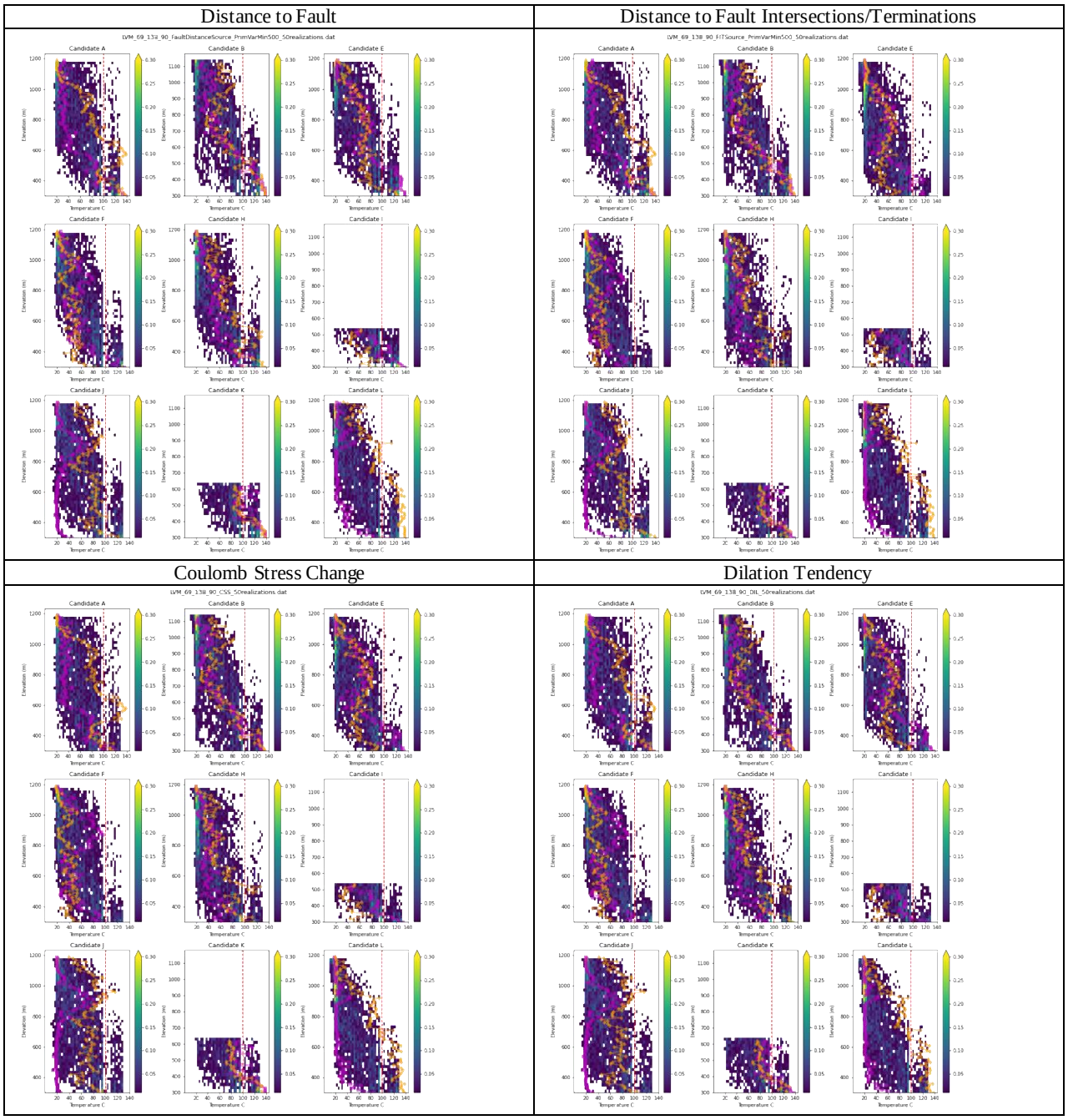

Figure 13: LVM results: vertical probability profiles at 9 candidate wells. Magenta and orange lines are from realization 25 and 49, respectively. Top row: Fault-based proxies. Bottom row: Stress-based proxies

3.5 V_{prior} & Entropy

Each of the candidate temperature probability profiles from above are summarized into two quantities: V_{prior} and entropy. The prior value is the expected outcome (weighted average) where higher temperatures have higher dollar amount ($), and entropy measures how distributed the probabilities are through the temperature bins (e.g., statistical disorder). First the cosimulation results are summarized, then the LVM results are presented for these two quantities. In order for an unbiased comparison of each profile, only the deepest ~250 m are used, which coincides with the simulated temperatures of Candidates I and K.

V_{prior} gives the likelihood of a high temperature outcome within the Granite Springs Valley. V_{prior} is calculated by using the probabilities of temperature and the nominal monetary amounts show in Figure 14 in Eq. 1 ($v_a(T)$). The important take away is that any utility function can be used and tailored for specific decision scenarios. Here we explain what the example monetary amounts could represent for our example utility function (Figure 14). Temperatures less than 45°C result in a monetary loss. In this case the temperatures would be so low that the developer might abandon the prospect, hence a total monetary loss. If temperatures between 45°C and 80°C are encountered, these temperatures may not be high enough to utilize for electricity generation, but they may be indicative of local convective hydrothermal circulation, though not in that particular TGH. Therefore this temperature outcome may have value in selecting the next drilling location(s). In this case the monetary result would be neutral since the data gained have some value. If temperatures greater than 80°C are encountered, there are profits to be made from geothermal development, and increasingly high temperature provides an increasing profit. Again, we emphasize that other values-temperature functions could be used to represent different risk attitudes and would change the V_{prior} results shown in this section.

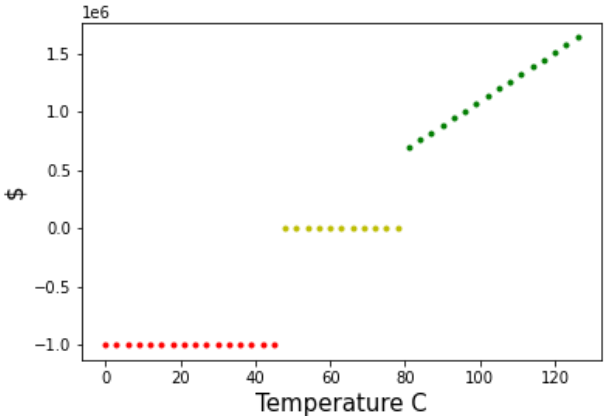

Figure 14: Value outcomes for drilling for economic temperatures, where temperatures <45°C result in loss, <80° is neutral, and >80° is an increasing profit

Table 4 contains the V_{prior} values for all the candidate well locations for the PCA1 Fault. The rankings are denoted in parentheses. Candidates B, E, and L have the highest potential for high temperatures, e.g., these candidate locations have the top three V_{prior} values and ranking. This can be explained by their orientation and relative proximity to measured temperatures greater than 90°C as shown in the last column of Table 4. Kriging system is such that the larger weights (λ_i) will be placed on the data values ($t(u)$) that align with the variogram's longest radius. The PCA1 Stress results are identical to those in Table 4; this is expected given the small differences in the stochastic models (Figure 12), and the further averaging that occurs in the V_{prior} calculation. Also of note is that four candidates have positive V_{prior}'s; those with negative V_{prior} indicates they have a majority of temperatures <40°C across the realizations.

Table 4: Cosimulation Vprior and entropy results with PCA1 Fault/Stress proxies as secondary data

	V_{PRIOR} *E+06 (rank)	Entropy (rank)	Map Distance (meters) to Nearest >90° Temperature	Azimuth to Nearest >90° Temperature Measurement
Candidate A	-9.37 (8)	3.80 (1)	1,396	14
Candidate B	7.26 (1)	2.68 (9)	630	227
Candidate E	6.31 (3)	3.33 (6)	2,124	262
Candidate F	-1.27 (5)	3.46 (5)	3,264	267
Candidate H	0.74 (4)	3.16 (7)	1,416	178
Candidate I	-5.99 (6)	3.66 (3)	1,447	240
Candidate J	-9.81 (9)	3.72 (2)	965	94
Candidate K	-8.67 (7)	3.48 (4)	3,398	254
Candidate L	6.37 (2)	2.95 (8)	4,482	261

Table 5 contains the V_{prior} results for the four different LVM groups, alongside the V_{prior} from cosimulation. Recall that V_{prior} (and entropy) are calculated only using the deepest 250 m, where Candidates I and K are defined, and LVM constrains the temperature means to be hotter deeper. Therefore, in general, V_{prior} is higher for the LVM than cosimulation results. Candidates A and B, on average, have the highest V_{prior} of the four LVM, however, we can see they are different depending on which of the four proxies are used. For cosimulation, Candidates B, E, and L have the highest likelihoods for hot temperatures.

Table 5: V_{prior} (10e+6) values for 9 candidate thermal gradient well locations for cosimulation (left) and four LVM (4 right most columns)

Candidate	Location	Cosim V_{PRIOR}	LVM Fault Distance	LVM Fault Terminations/ Intersections	LVM Coulomb Stress	LVM Dilations
A	north	-9.37	9.55	9.96	5.21	7.09
B	on fault	7.26	9.99	8.47	5.98	6.53
E	east middle	6.31	10.2	2.15	5.45	6.72
F	east middle	-1.27	9.12	3.63	4.42	6.17
H	east middle	0.743	9.43	4.79	3.76	6.76
I	west	-5.99	9.32	3.14	5.38	4.12
J	north	-9.81	6.29	7.73	3.2	3.99
K	west	-8.67	9.68	6.06	6.13	4.68
L	south west	6.37	8.48	7.14	5.45	4.78

Table 6: Entropy values for 9 candidate thermal gradiant well locations for cosimulation (left) and four LVM (4 right most columns)

Candidate	Location	Cosim Entropy	LVM Fault Distance	LVM Fault Terminations/ Intersections	LVM Coulomb Stress	LVM Dilations
A	north	3.80	4.03	3.99	4.42	4.23
B	on fault	2.68	4.06	4.27	4.49	4.45
E	east middle	3.33	4.04	4.48	4.38	4.24
F	east middle	3.46	4.11	4.46	4.36	4.3
H	east middle	3.16	4.16	4.5	4.54	4.31
I	west	3.66	4.03	4.32	4.26	4.3
J	north	3.72	4.42	4.24	4.57	4.58
K	west	3.48	4.05	4.34	4.28	4.42
L	south west	2.95	4.27	4.42	4.46	4.51

All candidate well locations are fairly close to a fault at these deeper depths, thus they are all green using "distance to fault" as an LVM. Candidate J is ranked lowest for all LVMs except fault terminations/intersections. Therefore, Candidate J is quite close to this geologic proxy and not the other three. Conversely, Candidate E is in the top three highest V_{prior} for all except fault terminations/intersections. LVM results show relatively higher V_{prior} for the western most wells (A, B, and K). If you consider Candidate J with intersections/terminations, it follows this pattern as well. It appears LVM, therefore, projects relatively high temperature down-dip (west) along the fault system despite wells A and K generally being location farther from the input temperature data (Table 4).

Entropy gives an indication of where new information could reduce statistical disorder the most. Entropy is calculated at each depth and averaged over the deepest 250 m of the profile (Eq. 2). Table 6 contains the entropy values and rankings for the cosimulation results (again the same for both Fault and Stress proxies for the same reason in V_{prior}). Candidate B has the lowest entropy due to its relative location to the existing temperature measurements (Table 4). A, J, and I have the top three highest entropy. Candidates A and J are on the northern outskirts of the measured temperature logs while I is located due west (Figure 2), therefore it is expected that they have higher entropies.

The LVM entropy values in Table 6 are higher than the cosimulation entropy values which can be attributed to the noisier spatial character of the LVM realizations. In the LVM results, Candidates J, L, and H have the highest entropies; H is surprising given that it is surrounded by temperature measurements. Therefore, this speaks of the proxy values being non-constraining or uninformative. The lowest are those using the distance to fault, which was the highest V_{prior} results of the four LVM.

Comparing Table 5 and Table 6, high entropy is never associated with high V_{prior}, since high entropy means there are significant probabilities in the lower temperature classes. A combination of low entropy (dark blue) and low V_{prior} (orange to red) should probably be ruled out for new wells as they represent more certain cooler locations. If considering the LVM fault distance results, Candidate I could represent this scenario. Conversely, Candidate H seems to be an interesting location for providing more information since it has relatively high entropy for all LVM cases, including cosimulation.

4.0 DISCUSSION

The clear advantage of LVM is that it produces more physically realistic representations by imposing a realistic temperature/depth relationship, and it removes the decision of how to represent the spatial density of measurements since they are needed exhaustively and thus require interpolation onto the simulation grid. Conversely, the high spatial frequencies in the LVM realizations produced are not as physically realistic, and therefore favor the two cosimulation realizations sets. Additionally, detailed studies should be performed to understand if anomalous upwellings could be systematically overshadowed by the geothermal gradient imposed by including depth in the regression.

Because cosimulation uses specific locations, the density at which these data are represented in the simulation grid are very consequential. This is a recognized challenge and both Koch et al. (2014) and Boyd et al. (2020) tested the sensitivity of the final uncertainty measures (like entropy) to different decimation factors of the secondary data. We performed some sensitivity studies to understand this sensitivity with different densities. In general, the V_{prior} and entropy values and rankings were similar until the secondary data were represented at the highest density (e.g., interpolated). In other words, when the secondary data are exhaustive, similar to how they are represented in the LVM realizations, the cosimulations have higher spatial frequencies (noisier characteristics) and therefore have higher entropy values like the LVM results. Although we found that the secondary data density was inconsequential to V_{prior} and entropy for most scenarios, the sensitivity study provided an additional observation to the LVM results that exhaustive data can create the high spatial frequencies, despite the fact that a Gaussian variogram with no nugget effect was imposed. Like the LVM probabilities, cosimulation with exhaustive secondary data have spread out probability profiles. If cosimulation is pursued for future geothermal drilling decisions, methods must be developed to better choose the secondary data density.

Cokriging, the basis of both cosimulation and LVM, shares all the contributions and limitations of kriging. Kriging provides a linear, least-squared error regression, combining data of diverse types accounting for their redundancy in space and their spatial correlation, as quantified by the variograms. The linear limitation of kriging may be more serious in cokriging, since cokriging would ignore any non-linear relation between two different attributes. We performed PCA transformation, which is considered a linear, orthogonal transformation. However, a non-linear transformation may be more appropriate for the four proxies given. Further analysis is needed to reveal if such non-linear dependence exists between the temperature data and the proxies.

We would like to emphasize there are many worthy scientific and economic motivations for drilling geothermal exploration wells, such as defining edges of the system and trying to retrieve the best geochemistry samples. The parameterization and uncertainty model would look very different for these two goals. Modeling of just the boundaries of the system or the geochemistry differences would need to be evaluated instead of continuous temperature. We believe that although the parameters would be different, the basic elements of this workflow could still be transferable for different drilling objectives.

5.0 CONCLUSIONS

The aim of this study was to use 3D uncertainty modeling of temperature to guide the decision for where to place new temperature wells, with the dual and not necessarily mutually exclusive purposes of confirming economic temperatures and/or reducing uncertainty about the conceptual understanding of the geothermal resource. For the current stage of Granite Springs Valley, the focus is on the understanding of the uncertainty of temperature in the subsurface, given the limited direct observations.

Two metrics were used to summarize the 3D stochastic temperature results address these two separate goals. V_{prior} was defined to place a higher value on hotter temperatures (Figure 14). Using high V_{prior} to determine new wells sites addresses the goal to confirm economic temperatures. Higher entropy locations can be ideal targets for placing wells with the purpose of increasing understanding about the geothermal resource.

To produce these 3D temperature models, we performed variogram analysis of the measured data in combination with the 3D geological model to determine the orientation and radii of the 3D ellipsoid, where the major direction of spatial correlation is in line with Fault 7 in the vicinity of the temperature measurements. Sequential simulation was utilized to produce 50 different models (realizations) that reproduced the measured temperatures at their respective 3D locations and also accounted for the spatial correlations represented by the 3D variogram ellipsoid.

The innovation explored in this paper was the inclusion of secondary data, where the secondary data are derived from the 3D geologic modeling. The four temperature proxies were distance to fault, distance to fault terminations and intersections, Coulomb stress change, and dilation tendency. Two methods were explored for including this information: cosimulation (stochastic cokriging) and LVM. In

practice, the LVM method fixes the mean temperature in a local neighborhood, while cosimulation treats the secondary data as secondary constraints at specific locations.

For cosimulation, first the correlation coefficients between the observed temperature data and four proxies were calculated to eliminate the need to calculate the cross variogram. The fault and stress proxies had very high correlations with each other, respectively, but none had higher magnitude than -0.56 (dilation) with the measured temperatures. It was decided to combine the two fault and two stress proxies via PCA for cosimulation. Cosimulation results using fault versus stress PCA1 produced nearly identical temperature models after their histograms were transformed, and therefore their V_{prior} and entropy summaries were equivalent. If the candidate locations were further away from the cluster of known temperatures, the influence of the secondary data will be more pronounced.

The LVM method requires an exhaustive representation of the mean temperature. The higher spatial frequencies again produce higher entropy values, but by including the depth in the linear regression and thus into the LVM, the temperature profiles generally increase with depth and therefore the V_{prior}'s are all positive. The V_{prior} values and rankings across the four LVM groups can vary given the location of candidate's location to the geologic proxies. With the exception of Candidates I and J, the LVM V_{prior} results show higher temperatures down dip of Fault 7 on the western side. But the V_{prior} for Candidate J is high using the fault intersection/terminations. The cosimulation results are more influenced by the primary data and thus the primary variogram and less on the patterns of the geologic proxies.

An improvement to this workflow would include increasing the depth of the model. Depending on the decision objectives, it may be more useful to represent production depths, and investigate where the highest (extrapolated temperatures) are put in the 3D subsurface, but the extrapolation methods would only be useful if guided by the secondary data proxies. Although these depths are far from measured temperatures, the secondary data could guide the simulated temperatures.

ACKNOWLEDGEMENTS

This work was authored by the National Renewable Energy Laboratory, operated by Alliance for Sustainable Energy, LLC, for the U.S. Department of Energy (DOE) under Contract No. DE-AC36-08GO28308. Funding provided by the U.S. Department of Energy Office of Energy Efficiency and Renewable Energy Geothermal Technologies Office. The views expressed in the article do not necessarily represent the views of the DOE or the U.S. Government. The U.S. Government retains and the publisher, by accepting the article for publication, acknowledges that the U.S. Government retains a nonexclusive, paid-up, irrevocable, worldwide license to publish or reproduce the published form of this work, or allow others to do so, for U.S. Government purposes.

This work is part of the INGENIOUS project funded by the U.S. Department of Energy Geothermal Technologies Office (award number DE-EE0009254).

REFERENCES

Ayling, B., Kirby, S., Hardwick, C., Kleeber, E., and Trainor-Guitton, W., 2022, INGENIOUS Phase 1 (budget period 1) progress report.:

Boyd, D.L., Walton, G., and Trainor-Guitton, W., 2020, Geostatistical estimation of Ground Class prior to and during excavation for the Caldecott Tunnel Fourth Bore project: Tunnelling and Underground Space Technology, v. 100, p. 103391, doi: 10.1016/j.tust.2020.103391.

Chilès, J.-P., and Delfiner, P., 2012, Geostatistics: Modeling Spatial Uncertainty: Second Edition:

Craig, J.W., Faulds, J.E., Hinz, N.H., Earney, T.E., Schermerhorn, W.D., Siler, D.L., Glen, J.M., Peacock, J., Coolbaugh, M.F., and Deoreo, S.B., 2021, Discovery and analysis of a blind geothermal system in Southeastern Gabbs valley, Western Nevada, USA: Geothermics, v. 97, doi: 10.1016/j.geothermics.2021.102177.

Cumming, W., 2016a, Resource Capacity Estimation Using Lognormal Power Density from Producing Fields and Area from Resource Conceptual Models; Advantages, Pitfalls and Remedies, *in* PROCEEDINGS, 41st Workshop on Geothermal Reservoir EngineeringStanford University, Stanford, California, February 22-24,.

Cumming, W., 2016b, Resource Conceptual Models of Volcano-Hosted Geothermal Reservoirs for Exploration Well Targeting and Resource Capacity Assessment: Construction, Pitfalls and Challenges.:

Deutsch, C. V., and Journel, A.G., 1998, GSLIB: Geostatistical Software Library and User's Guide.: New York, Oxford University Press.

Faulds, J.E., Coolbaugh, M.F., Benoit, D., Oppliger, G., Perkins, M., Moeck, I., and Drakos, P., 2010, Structural Controls of Geothermal Activity in the Northern Hot Springs Mountains, Western Nevada: The Tale of Three Geothermal Systems (Brady's, Desert Peak, and Desert Queen): Geothermal Resources Council Transactions, v. 34, p. 675–683.

Faulds, J., Hinz, N., Coolbaugh, M.F., Ayling, B.F., Faulds, J.E., Hinz, N.H., Ramelli, A.R., Glen, J.M., Wannamaker, P.E., Deoreo, S., Siler, D.L., and Craig, J.W., 2019, Vectoring into Potential Blind Geothermal Systems in the Granite Springs Valley Area, Western Nevada: Application of the Play Fairway Analysis at Multiple Scales, *in* PROCEEDINGS, 44th Workshop on Geothermal Reservoir Engineering Stanford University, Stanford, California, February 11-13, 2019 SGP-TR-214,.

Faulds, J.E., Hinz, N.H., Coolbaugh, M.F., DePolo, C.M., Siler, D.L., Shevenell, L.A., Hammond, W.C., Kreemer, C., and Queen, J.H., 2015a, Discovering Blind Geothermal Systems in the Great Basin Region : An Integrated Geologic and Geophysical Approach for Establishing Geothermal Play Fairways.:

Faulds, J.E., Hinz, N.H., Coolbaugh, M.F., Sadowski, A.J., Shevenell, L.A., Mcconville, E., Craig, J., Sladek, C., and Siler, D.L., 2017, Progress Report on the Nevada Play Fairway Project: Integrated Geological, Geochemical, and Geophysical Analyses of Possible New Geothermal Systems in the Great Basin Region, *in* Proceedings, 42nd Workshop on Geothermal Reservoir Engineering, Stanford University,.

Faulds, J.E., Hinz, N.H., Coolbaugh, M.F., Shevenell, L.A., Siler, D.L., Craig, M., Hammond, W.C., Kreemer, C., Oppliger, G., Wannamaker, P.E., Queen, J.H., and Visser, C.F., 2015b, Integrated Geologic and Geophysical Approach for Establishing Geothermal Play Fairways and Discovering Blind Geothermal Systems in the Great Basin Region , Western USA : A Progress Report: Geothermal Research Council Transactions, v. 39, p. 691–700.

Gloaguen, E., Marcotte, D., Chouteau, M., and Perroud, H., 2005, Borehole radar velocity inversion using cokriging and cosimulation: Journal of Applied Geophysics, v. 57, p. 242–259, doi: 10.1016/j.jappgeo.2005.01.001.

Gloaguen, E., Marcotte, D., Giroux, B., Dubreuil-Boisclair, C., Chouteau, M., and Aubertin, M., 2007, Stochastic borehole radar velocity and attenuation tomographies using cokriging and cosimulation: Journal of Applied Geophysics, v. 62, p. 141–157, doi: 10.1016/j.jappgeo.2006.10.001.

Hansen, T.M., Journel, A.G., Tarantola, A., and Mosegaard, K., 2006, Linear inverse Gaussian theory and geostatistics: Geophysics, v. 71.

Jotta Ariza Ferreira, D., and Moreira Lupinacci, W., 2018, An approach for 3D quantitative carbonate reservoir characterization in the Pampo field, Campos Basin, offshore Brazil: AAPG Bulletin, v. 11, p. 2267–2282, doi: 10.1306/04121817352.

Journel, A., and Huijbregts, C., 1978, Mining geostatistics: London, Academic Press, 600 p.

Koch, J., He, X., Jensen, K.H., and Refsgaard, J.C., 2014, Challenges in conditioning a stochastic geological model of a heterogeneous glacial aquifer to a comprehensive soft data set: Hydrology and Earth System Sciences, v. 18, p. 2907–2923, doi: 10.5194/hess-18-2907-2014.

Remy, N., Boucher, A., and Wu, J., 2011, Applied Geostatistics with SGeMS: A User's Guide: Cambridge University Press, 264 p.

Siler, D.L., and Faulds, J.E., 2013, Three-Dimensional Geothermal Fairway Mapping: Examples From the Western Great Basin , USA: GRC Transactions, v. 37, p. 327–332.

Siler, D.L., Hinz, N.H., and Faulds, J.E., 2018, Stress concentrations at structural discontinuities in active fault zones in the western United States: Implications for permeability and fluid flow in geothermal fields: Bulletin of the Geological Society of America, v. 130, p. 1273–1288, doi: 10.1130/B31729.1.

Siler, D.L., and Pepin, J.D., 2021, 3-D Geologic Controls of Hydrothermal Fluid Flow at Brady geothermal field, Nevada, USA: Geothermics, v. 94, p. 102112, doi: 10.1016/j.geothermics.2021.102112.

Webster, R., and Oliver, M.A., 2008, Geostatistics for Environmental Scientists: Second Edition: 1–315 p.

Williams, C., and DeAngelo, C., 2011, Evaluation of Approaches and Associated Uncertainties in the Estimation of Temperatures in the Upper Crust of the Western United States: Geothermal Research Council Transactions, v. 35, p. 1599–1606.

Witter, J.B., Trainor-Guitton, W.J., and Siler, D.L., 2019, Uncertainty and risk evaluation during the exploration stage of geothermal development: A review: Geothermics, v. 78, p. 233–242, doi: 10.1016/j.geothermics.2018.12.011.